PRELIMINARY RESULTS OF A DISCONTINUOUS GALERKIN IMMERSED BOUNDARY METHOD COMBINING PENALIZATION AND ANISOTROPIC MESH ADAPTATION

MARCO LORINI[1], CECILE DOBRZYNSKI[1], VINCENT PERRIER[2] AND MARIO RICCHIUTO[1]

[1] Inria Bordeaux Sud-Ouest, Team CARDAMOM,
200 rue Vieille Tour, 33405 Talence, France,
marco.lorini@inria.fr, cecile.dobrzynski@inria.fr, mario.ricchiuto@inria.fr

[2] Inria Bordeaux Sud-Ouest, team CAGIRE and LMAP UMR CNRS 5142,
Université de Pau et des Pays de l'Adour, Avenue de l'Université 64013 Pau, France,
vincent.perrier@inria.fr

Key words: Immersed Boundary Method, Penalized Navier-Stokes equations, Anisotropic Mesh Adaptation, Discontinuous Galerkin

Abstract. We propose an Immersed Boundary Method in which the wall boundary conditions are taken into account through a penalization technique, *i.e.* through the addition of a source term to the Navier-Stokes equations. The localization of the solid bodies inside the domain is done via a level-set method, employing the signed distance function. We discretize the resulting equations with a Discontinuous Galerkin approach. With the combination of anisotropic mesh adaptation and unstructured simplicial meshes, the accuracy of the definition of the solid boundaries, not explicitly discretized, can be improved without increasing too much the computational cost of the simulation.

1 INTRODUCTION

Immersed Boundary Methods (IBM) are nowadays an attractive alternative to the classical body-fitted approach, mainly because they greatly simplify the mesh generation process, especially in the case of moving bodies. For body-fitted grids, the solid wall boundaries are meshed and boundary conditions are imposed through additional equations. On the contrary, IBM are characterised by a mesh that covers the entire domain, not conforming to the geometry of the immersed boundaries.

A modification of the equations in the vicinity of the bodies is then needed to properly incorporate the boundary conditions. The penalization technique [1, 2, 3] is an IBM in which the wall boundary conditions are taken into account through the addition of source terms to the governing equations. The bodies are described using the level-set method, employing the signed distance function (SDF) as a level-set. As a consequence, a solid body is located on the mesh by the zero-isovalue of the SDF.

We propose here to solve the penalized compressible Navier-Stokes equations using a Discontinuous Galerkin (DG) scheme on adapted grids. DG methods [4] are finite element methods in which the solution of the variational form of a problem is approximated by piecewise polynomial functions with no global continuity requirement. Nowadays they are finding use in very diverse applications because of their robustness, accuracy and geometrical flexibility. These aspects combined with the compactness of the scheme have been advantageous for the parallel implementation of the proposed method.

The accuracy of the definition of the solid boundaries, not explicitly discretized, depends on the mesh size used. Since a uniform refinement would be inefficient producing finer areas where not necessary (*i.e.* far from the body), a more flexible approach is to improve the representation of the bodies combining anisotropic mesh adaptation and unstructured simplicial meshes. Anisotropic mesh adaptation has largely proved useful in the context of numerical simulations to capture the physical behavior of a complex phenomenon at a reasonable computational cost [5]. Here we are interested in adapting the mesh to both the level-set and some relevant physical variable or flow feature, in order to have a better accuracy with a smaller number of elements. Furthermore, highly-stretched anisotropic elements introduce regularity in the approximation of the immersed boundaries and allow to insert fewer elements in the refined areas.

In the following, the method is presented and particular attention is paid to the mesh adaptation strategy employed. Results on benchmark two- and three-dimensional test cases are then presented to show the promising features of the method.

2   GOVERNING EQUATIONS

Being an IBM, penalization is characterized by a mesh covering the entire domain. The solid is considered as a porous media, with a very small intrinsic permeability, based on an idea introduced by Brinkman [6]. The velocity field is extended inside the solid and the Navier-Stokes equations are solved with a penalization term to enforce rigid motion inside the body, leading to the so-called Penalized Navier-Stokes or Brinkman-Navier-Stokes equations:

$$\frac{\partial \rho}{\partial t} + \frac{\partial}{\partial x_j}(\rho u_j) = 0 \tag{1}$$

$$\frac{\partial}{\partial t}(\rho u_i) + \frac{\partial}{\partial x_j}(\rho u_j u_i) = -\frac{\partial p}{\partial x_i} + \frac{\partial \tau_{ji}}{\partial x_j} - \frac{1}{\eta_p}\sum_{n=1}^{N_s}\chi_{s^n}(\rho u_i - \rho u_i^{s^n}) \tag{2}$$

$$\frac{\partial}{\partial t}(\rho E) + \frac{\partial}{\partial x_j}(\rho u_j H) = \frac{\partial}{\partial x_j}\left[u_i \tau_{ij} - q_j\right] - \frac{1}{\eta_p}\sum_{n=1}^{N_s}\chi_{s^n}(\rho u_i - \rho u_i^{s^n})u_i \tag{3}$$

$$- \frac{1}{\eta_p}\sum_{n=1}^{N_s}\theta_{s^n}\chi_{s^n}(\rho e - \rho e^{s^n})$$

The total energy, the total enthalpy, the pressure, the stress tensor and the heat flux vector are given by:

$$E = e + u_k u_k / 2, \tag{4}$$

$$H = h + u_k u_k / 2, \tag{5}$$

$$p = (\gamma - 1)\rho e, \tag{6}$$

$$\tau_{ij} = 2\mu \left[S_{ij} - \frac{1}{3} \frac{\partial u_k}{\partial x_k} \delta_{ij} \right], \tag{7}$$

$$q_j = -\frac{\mu}{Pr} \frac{\partial h}{\partial x_j}, \tag{8}$$

where e is the internal energy, h the enthalpy, γ the ratio of gas specific heats, Pr the molecular Prandtl number and

$$S_{ij} = \frac{1}{2} \left(\frac{\partial u_i}{\partial x_j} + \frac{\partial u_j}{\partial x_i} \right) \tag{9}$$

is the mean strain-rate tensor.

Regarding the parameters of the penalization terms, N_s corresponds to the number of solids s^n considered inside the domain and θ_{s^n} gives the possibility to penalize the energy (Dirichlet boundary condition, $\theta_{s^n} = 1$) or not (Neumann boundary condition, $\theta_{s^n} = 0$). The quality of the penalization depends on the choice of the penalization parameter η_p, that has to be chosen small enough to ensure $\frac{1}{\eta_p} \gg 1$. In all the simulations presented here we employed an implicit scheme with $\eta_p = 10^{-10}$. Finally, χ_{s^n} is the characteristic function of the solid s^n, namely:

$$\chi_{s^n} = H\left(-\Phi_{s^n}\right), \tag{10}$$

where H is the Heaviside function and Φ_{s^n} is the signed distance function to the boundary of s^n. Looking at Eqs. (1–3), the summation terms are responsible for the enforcement of the boundary conditions at the solid walls and inside the solid. Indeed, outside the solids the χ_{s^n} functions are equal to 0, so that the penalization terms vanish and the usual Navier-Stokes equations are recovered. On the opposite, inside a solid, the characteristic function is equal to 1 and the coefficient $\frac{1}{\eta_p}$ makes those terms dominate, imposing the boundary values.

3 DISCONTINUOUS GALERKIN DISCRETIZATION

The governing equations can be written in compact form as

$$\frac{\partial \mathbf{u}}{\partial t} + \boldsymbol{\nabla} \cdot \mathbf{F}_c(\mathbf{u}) + \boldsymbol{\nabla} \cdot \mathbf{F}_v(\mathbf{u}, \boldsymbol{\nabla}\mathbf{u}) + \mathbf{p}(\mathbf{u}) = \mathbf{0} \tag{11}$$

where $\mathbf{u} \in \mathbb{R}^m$ denotes the vector of the m conservative variables, $\mathbf{p} \in \mathbb{R}^m$ the penalization term, d the space dimension, $\mathbf{F}_c, \mathbf{F}_v \in \mathbb{R}^m \otimes \mathbb{R}^d$ the inviscid and viscous flux functions.

A weak formulation of Eq. (11) is obtained multiplying each scalar law by an arbitrary smooth test function $v_j \in \mathbf{v}$, $1 \le j \le m$, and integrating by parts:

$$\int_\Omega v_j \frac{\partial u_j}{\partial t} \, \mathrm{d}\mathbf{x} - \int_\Omega \boldsymbol{\nabla} v_j \cdot \mathbf{F}_j(\mathbf{u}, \boldsymbol{\nabla}\mathbf{u}) \, \mathrm{d}\mathbf{x}$$
$$+ \int_{\partial\Omega} v_j \mathbf{F}_j(\mathbf{u}, \boldsymbol{\nabla}\mathbf{u}) \cdot \mathbf{n} \, \mathrm{d}\sigma + \int_\Omega v_j \mathbf{p}_j(\mathbf{u}) \, \mathrm{d}\mathbf{x} = 0, \quad (12)$$

where $\mathbf{F}_j$ is the sum of the inviscid and viscous flux vectors, Ω the computational domain, $\partial\Omega$ the boundary of Ω, $\mathbf{n}$ the unit normal vector to the boundary.

Let Ω_h be an approximation of the domain $\Omega \in \mathbb{R}^d$, $\mathcal{T}_h = \{K\}$ a mesh of Ω_h, *i.e.* a collection of "finite elements" K, $\mathcal{F}_h = \{F\}$ the mesh faces, and let $\mathbf{V}_h$ denotes a discontinuous finite element space spanned by polynomial functions continuous only inside each element K, *i.e.*

$$\mathbf{V}_h \overset{\text{def}}{=} \left[\mathbb{P}_d^l(\mathcal{T}_h) \right]^m, \quad (13)$$

where

$$\mathbb{P}_d^l \overset{\text{def}}{=} \{v_h \in L^2(\Omega_h) : v_h|_K \in \mathbb{P}_d^l, \forall K \in \mathcal{T}_h\} \quad (14)$$

is the space of polynomials of degree at most l on the element K. The solution $\mathbf{u}$, the test function $\mathbf{v}$ are replaced with finite element approximations $\mathbf{u}_h$ and $\mathbf{v}_h$, belonging to the space $\mathbf{V}_h$. The DG formulation of the problem (12) requires to find $\mathbf{u}_h \in \mathbf{V}_h$ such that

$$\sum_{K \in \mathcal{T}_h} \int_K v_{h,j} \frac{\partial u_{h,j}}{\partial t} \, \mathrm{d}\mathbf{x} - \sum_{K \in \mathcal{T}_h} \int_K \boldsymbol{\nabla}_h v_{h,j} \cdot \mathbf{F}_j\left(\mathbf{u}_h, \boldsymbol{\nabla}_h \mathbf{u}_h + \mathbf{r}(\llbracket \mathbf{u}_h \rrbracket)\right) \, \mathrm{d}\mathbf{x}$$
$$+ \sum_{F \in \mathcal{F}_h} \int_F \llbracket v_{h,j} \rrbracket \cdot \widehat{\mathbf{f}}_j\left(\mathbf{u}_h^\pm, (\boldsymbol{\nabla}_h \mathbf{u}_h + \eta_F \mathbf{r}_F(\llbracket \mathbf{u}_h \rrbracket))^\pm\right) \, \mathrm{d}\sigma$$
$$+ \sum_{K \in \mathcal{T}_h} \int_K v_{h,j} \mathbf{p}_j(\mathbf{u}_h) \, \mathrm{d}\mathbf{x} = \mathbf{0}$$
$$\mathbf{v}_h \in \mathbf{V}_h, \quad (15)$$

where $\mathbf{r}$ and $\mathbf{r}_F$ are the global and the local lifting operators and η_F is a stability parameter [7]. The numerical flux function $\widehat{\mathbf{f}}$, appearing in the boundary integral of Eq. (15), uniquely defines the flux at the elements interfaces and prescribes the boundary data on the discretized boundaries. Indeed, the flux $\widehat{\mathbf{f}}$ is the sum of an inviscid, $\widehat{\mathbf{f}}_c$, and a viscous, $\widehat{\mathbf{f}}_v$, contribution. For the former we chose a Lax-Friedrichs scheme while for the latter the BR2 scheme [8] was employed.

4 MESH ADAPTATION

In general, a mesh adaptation method uses an error estimate to convert the approximation error into a piece of information to be used by the other stages of the adaptation procedure. In the case of h-adaptation, this information is used to locally prescribe the size and the orientation of the mesh elements. Once a numerical solution is obtained on a

given mesh, the aim is to equidistribute the approximation error over the mesh by locally adjusting the mesh density, according to an a posteriori correlation.

As proposed in [9], we used a metric tensor field based on the Hessian of the numerical solution to prescribe sizes and direction of the adapted mesh. These metrics are positive definite symmetric matrices defined in each node of the mesh. Being diagonalizable, the eigenvalues λ_i of these matrices are directly linked to the sizes h_i of the elements edges in the directions i (where $\lambda_i = 1/h_i^2$), with these directions given by the eigenvectors. Furthermore, anisotropic meshes are used to highly stretch elements (triangles or tetrahedra) in order to limit the number of elements in refined areas.

We chose two different criteria for mesh adaptation, thus producing two different metrics defined at each mesh point. A single metric is then obtained intersecting the two, exploiting the simultaneous reduction method [9].

4.1 Level-set adaptation

As explained in Sec.1, an immersed solid is located on the mesh thanks to the SDF. In order to define more precisely the boundary and to impose penalization in an accurate way, a refinement of the mesh in the region close to the solid boundary was exploited. It has been shown in [10] that to adapt with respect to the zero-isovalue of the level-set the following metric can be employed:

$$\mathcal{M} = {}^t\mathcal{R} \begin{pmatrix} \frac{1}{\epsilon^2} & 0 & 0 \\ 0 & \frac{|\lambda_1|}{\epsilon} & 0 \\ 0 & 0 & \frac{|\lambda_2|}{\epsilon} \end{pmatrix} \mathcal{R} \tag{16}$$

where $\mathcal{R} = (\nabla\Phi \; v_1 \; v_2)$, $(v_1, \; v_2)$ is a base of the tangential plane of the surface defined by the isovalues of the SDF, Φ, and λ_i are the eigenvalues of the Hessian of Φ. The parameter ϵ is the allowed error in the approximation of the SDF and this metric is imposed only in a vicinity w of the surface.

4.2 Physical adaptation

Indeed, mesh adaptation allows to refine the mesh in order to better represent some physical phenomena of interest. For such a kind of adaptation, the aim is to control the interpolation error between the exact solution u and its interpolant $\Pi_h u$ on the actual mesh. An upper bound for this error on a mesh element K is given by [5]:

$$||u - \Phi_h u||_{\infty,K} \leq c_d \max_{\mathbf{e} \in K} \langle \mathbf{e}, \mathcal{M}(K)\mathbf{e} \rangle \; . \tag{17}$$

Here, $\mathbf{e}$ denotes the edges of the mesh element, c_d is a constant depending on the dimension and the metric $\mathcal{M}(K)$ is computed with the Hessian of u, $\mathcal{H}_u$:

$$\mathcal{M} = {}^t\mathcal{R} \begin{pmatrix} \lambda_1 & 0 & 0 \\ 0 & \lambda_2 & 0 \\ 0 & 0 & \lambda_3 \end{pmatrix} \mathcal{R} \tag{18}$$

5

where $\mathcal{R}$ is the matrix of the eigenvectors of $\mathcal{H}_u$ and the λ_i are defined as:

$$\lambda_i = \min\left(\max\left(|h_i|, \frac{1}{h_{max}^2}\right), \frac{1}{h_{min}^2}\right) . \tag{19}$$

with h_{min} (resp. h_{max}) the minimum (resp. maximum) size allowed for the mesh edges and h_i the eigenvalues of $\mathcal{H}_u$.

5   RESULTS

For each test case, the adaptation criteria and parameters were left unchanged throughout the procedure. Starting from an initial mesh, once a first numerical solution was computed, we applied the mesh adaptation procedure described in Sec.4 and the solution was later re-evaluated. Usually 2-3 iterations were needed for the convergence of the mesh adaptation algorithm.

All the computations were run in parallel, initializing the $\mathbb{P}^0$ solution from the uniform flow at inflow conditions and the higher-order solutions from the lower-order ones.

5.1   2D: Flow around NACA0012 airfoil

The first test case presented is the laminar viscous flow around a NACA0012 airfoil, in a subsonic and a transonic configuration. For the subsonic case, the Reynolds number was set to $Re = 5000$, the Mach number to $M = 0.5$ and we set zero angle of attack. For the transonic case, the Reynolds number was set to $Re = 73$, the Mach number to $M = 0.8$ and the angle of attack to $\alpha = 10°$.

We computed both the configurations on the same mesh, that was adapted for the subsonic case to both the level-set and the pressure distribution. The adaptation parameters adopted were kept constant during the adaptation procedure (3 iterations) and are reported in Tab. 1.
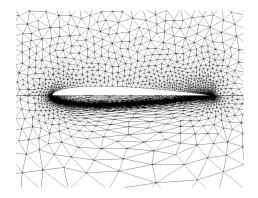

Figure 1: Adapted meshes for the NACA0012 test cases. *Upper half*: body-fitted approach, *lower half*: embedded approach.

Table 1: Adaptation parameters for the subsonic NACA0012 test case.

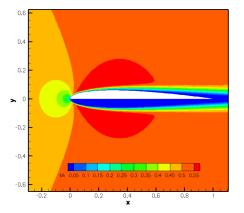| Variable	ϵ	h_{min}	h_{max}
0-isovalue	0.001	0.001	2
p	0.001	0.01	2

Figure 2: Mach number distribution for the subsonic NACA0012 test case, $\mathbb{P}^4$ approximation. *Upper half*: body-fitted approach, *lower half*: embedded approach.
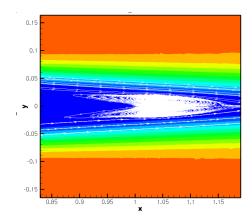

Figure 3: Mach number distribution and streamlines around the trailing edge for the subsonic NACA0012 test case, $\mathbb{P}^4$ approximation, embedded approach.

To validate the proposed approach we first computed a solution on a body-fitted mesh adapted 3 times, and then compared the results with the ones obtained with the IBM. The 6676 elements body-fitted mesh and the 10732 elements embedded mesh are presented in Fig. 1.

In Fig. 2 the Mach number distributions of both the approaches are compared for a $\mathbb{P}^4$ approximation. In Fig. 3, a close-up around the trailing edge of the profile shows that the IBM correctly reproduced the steady separation bubble, that is a distinctive feature of this test case.

The results for the transonic configuration are presented in Fig. 4 and 5, where again the Mach number distributions for both the approaches are depicted.

5.2 3D: Flow past a sphere

To test our method in 3D we chose a well-known benchmark test case, the viscous laminar flow past a sphere. Calculations for Reynolds numbers of up to 200 have shown a steady axisymmetric flow topologically independent from the Reynolds number. The flow is seen to separate from the surface of the sphere at an angle of separation, θ_s, evaluated from the stagnation point and re-attach at a point x_s on the axis of the flow, forming a closed separation bubble. This bubble is characterized by toroidal vortices
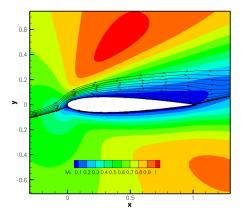
Figure 4: Mach number distribution and streamlines for the transonic NACA0012 test case, $\mathbb{P}^4$ approximation, body-fitted approach.
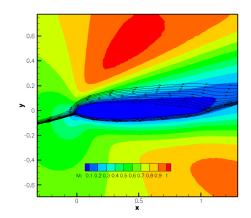

Figure 5: Mach number distribution and streamlines for the transonic NACA0012 test case, $\mathbb{P}^4$ approximation, embedded approach.

centred at coordinates (x_c, y_c), defined as the points in which the velocity is zero in the sphere's reference frame. Increasing the Reynolds number up to 200 doesn't affect the flow structure, but changes the separation location, the vortex center location and the separation length.

In our computations, we set the Reynolds number to $Re = 150$, the Mach number to $M = 0.1$ and no angle of attack. As before, we first computed the case on a body-fitted mesh adapted with same parameters as the embedded one (which are reported in Tab. 2). A cut of the resulting embedded mesh is depicted in Fig. 6, while Fig. 7 shows the localization of the sphere on the same mesh.
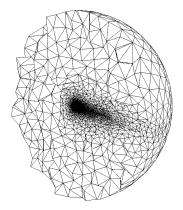

Figure 6: Cut of the 3D mesh for the sphere test case, showing the refined region after 3 iterations of adaptation.
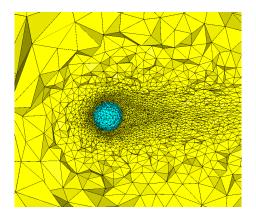

Figure 7: Localization of the sphere in the adapted mesh. *Yellow*: positive values of the SDF, *blue*: negative values of the SDF.

8

Table 2: Adaptation parameters for the sphere test case.

Variable	ϵ	h_{min}	h_{max}
0-isovalue	0.002	0.04	2.5
M	0.002	0.04	2.5

In Fig. 8 the Mach number distribution for both the approaches are compared and in Fig. 9 the streamlines for the embedded approach show the steady separation bubble. Finally, in Tab.3 we compared the geometrical parameters of the bubble with the literature reference data.

Table 3: Geometry of the steady separation bubble.

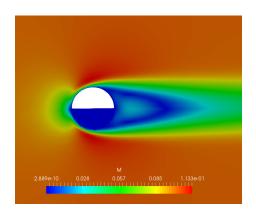|	θ_s	x_s	x_c	y_c
IBM $\mathbb{P}^2$	127°	1.74	0.86	0.34
Ref. data [11]	124°	1.7	0.8	0.32

Figure 8: Mach number at a mid-plane slice of the sphere, $\mathbb{P}^2$ approximation. *Upper half*: body-fitted, *lower half*: embedded.

Figure 9: Streamlines along the separation region at a mid-plane slice of the sphere, $\mathbb{P}^2$ approximation, embedded approach.

6 CONCLUSIONS

The Penalized Navier-Stokes equations have been solved using a Discontinuous Galerkin method and mesh adaptation has been employed to improve the accuracy of the solid definition. The reason is twofold. First, keep the simplicity of the penalization method in computing flow solutions around complex geometries, simplifying the mesh generation process. Secondly, overcome the well-known difficulties of embedded approaches in the wall treatment.

Mesh adaptations have been performed using two criteria: the distance to the zero-isovalue of the level-set and a physical variable of the flow solution (p or M in our case). The proposed 2D and 3D test cases demonstrated the ability of the method to obtain an accurate solution even when the mesh does not contain a priori any point on the zero-isovalue of the level-set. For a given accuracy, the number of elements added by the adaptation procedure to the IBM mesh is clearly larger than the one for its body-fitted counterpart, but still of the same order.

The next step will be to extend the method to the case of moving bodies as well as for turbulent flows computations.

REFERENCES

[1] P. Anglot, C.-H. Bruneau and P. Fabrie. A penalization method to take into account obstacles in incompressible viscous flows. *Numer. Math.* (1999) **81**:497–520.

[2] R. Abgrall, H. Beaugendre and C. Dobrzynski. An immersed boundary method using unstructured anisotropic mesh adaptation combined with level-sets and penalization techniques. *Journal of Computational Physics* (2014) **257**:83–101.

[3] L. Nouveau, H. Beaugendre, C. Dobrzynski, R. Abgrall and M. Ricchiuto. An adaptive, residual based, splitting approach for the penalized Navier Stokes equations. *Comput. Methods Appl. Mech. Engrg.* (2016) **303**:208–230.

[4] F. Bassi and S. Rebay. A high-order accurate discontinuous finite element method for the numerical solution of the compressible Navier–Stokes equations. *Journal of Computational Physics* (1997) **131**(2):267–279.

[5] P.J. Frey and F. Alauzet. Anisotropic mesh adaptation for CFD computations. *Comput. Methods Appl. Mech. Engrg.* (2005) **194**:5068–5082.

[6] H.C. Brinkman. A calculation of the viscous force exerted by a flowing fluid on a dense swarm of particles. *Appl. Sci. Res.* (1949) **1**:27–34.

[7] D.N. Arnold, F. Brezzi, B. Cockburn and D. Marini. Unified analysis of discontinuous Galerkin methods for elliptic problems. *SIAM J. Numer. Anal.* (2002) **39**:1749–1779.

[8] F. Bassi, S. Rebay, G. Mariotti, S. Pedinotti and M. Savini. A high-order accurate discontinuous finite element method for inviscid and viscous turbomachinery flows. In: R. Decuypere and G. Dibelius. *Proceedings of the 2nd European Conference on Turbomachinery Fluid Dynamics and Thermodynamics* (1997) 99–108.

[9] P.J. Frey and P.L. George. *Mesh generation. Application to finite elements.* Wiley, 2nd edition, 2008.

[10] C. Dapogny and P.J. Frey. Computation of the signed distance function to a discrete contour on adapted triangulation. *Calcolo* (2012) **49**:193–219.

[11] T.A. Johnson and V.C. Patel. Flow past a sphere up to a Reynolds number of 300. *J. Fluid Mech.* (1999) **378**:19–70.